44th AIAA Aerospace Sciences Meeting and Exhibit
9 - 12 January 2006, Reno, Nevada

AIAA 2006-1526

# The First High-Order CFD Simulation of Aircraft: Challenges and Opportunities

Foluso Ladeinde*, Ken Alabi†, Cosmin Safta‡, and Xiaodan Cai §
*Thaerocomp Technical Corporation, P.O. Box 1527, Stony Brook, NY 11790-0609*

Forrester Johnson**
*The Boeing Company, P.O. Box 3707, MC 67-LH, Seattle, WA 98124-2207*

**The textbook advantages of high-order differencing schemes in computational fluid dynamics (CFD) are well documented. They have also been demonstrated in the literature, albeit for canonical problems. The objective of the work described in this paper is to provide a robust implementation of high-order schemes to permit high fidelity and routine simulation of realistic aerospace systems which usually involve very complex geometries and flow behaviors. The two high-order schemes we have implemented are the compact and weighted essentially non-oscillatory (WENO) schemes. Some challenges were encountered in our efforts to accomplish the foregoing objective. Detailed illustrations of the various challenges are provided, as are some remedies that we have proposed and successfully implemented. This then allows us to illustrate some of the potential advantages of high-order methods for the simulation of realistic aerospace applications. The roles that the authors envision for high-order methods in CFD simulation of realistic aerospace systems are also discussed.**

## Nomenclature

| | | |
|---|---|---|
| $C_p$ | = | pressure coefficient or specific heat at constant pressure |
| $D$ | = | van Driest damping function |
| $dt$ | = | time step size |
| $e$ | = | internal energy |
| $E$ | = | total specific energy |
| $H_i^{SGS}$ | = | $i^{\text{th}}$ component of the sub-grid scale heat flux vector |
| $h$ | = | enthalpy |
| $J$ | = | Jacobian of the coordinate transformation matrix |
| $k$ | = | kinetic energy |
| $\text{Pr}_T$ | = | turbulence Prandtl number |
| $Q$ | = | vector of conserved variables |
| $S$ | = | source term in the flow-energy equations |
| $S_{ij}$ | = | "$ij$" component of the strain rate tensor |
| $t$ | = | time |
| $u, v, w$ | = | velocity components in the $x, y, z$ Cartesian coordinate directions, respectively |
| $u_\tau$ | = | friction velocity |
| $(x, y, z)$ | = | the Cartesian coordinate directions |
| $y^+$ | = | shortest distance to the nearest wall normalized by the friction velocity and fluid kinematic |

* Director of Research, AIAA Life Member and Associate Fellow
† Research Engineer, AIAA Member
‡ Research Engineer, AIAA Member
§ Senior Research Engineer, AIAA Member
** Senior Technical Fellow, Aerodynamics Research Engineering, AIAA Fellow

viscosity

$\mu_T, \nu_T$ = turbulence dynamic and kinematic viscosities, respectively

$\Delta$ = grid size

$\rho$ = fluid density

$\varepsilon$ = turbulence kinetic energy dissipation rate

$\tau_{ij}$ = the "*ij*" component of the shear stress tensor

$(\xi, \eta, \zeta)$ = the curvilinear coordinate directions

$( )^{SGS}$ = sub-grid scale value of the quantity indicated by "( )"

## I. Introduction

The accurate solutions of a broad spectrum of dynamic, multi-physics phenomena, such as turbulence, aeroacoustics, fluid/structure interaction, and electromagnetics, still pose some challenges for computational fluid dynamics (CFD). High-order methods have been proposed as a way to produce highly-accurate results and reduce the severe computational requirements of standard low-order methods.[1-7] High-order procedures based on the compact schemes[2,8,9] have been proposed for reducing dispersion and isotropy errors, and the superior accuracy of the procedures over low-order methods has been demonstrated.[8,10,28] The spectral-like resolution of compact schemes[2] and the ease of extension to multiple disciplines are other attractive features of the method.

Although recent work by Visbal and co-workers has extended the compact schemes for application in high Mach number flows, the procedure is still only well-suited for incompressible and low Mach number flows. High-order calculations based on the essentially non-oscillatory (ENO)[4] and the weighted essentially non-oscillatory (WENO)[5-7] procedures are more appropriate for high Mach number flows. WENO is an improvement over ENO in four respects that are listed on page 16 of Shu.[7] For this reason, the present work focuses on WENO for high Mach number calculations. Hybrid procedures combining compact and ENO schemes have also received attention.[11]

The application of these high-order methods to realistic aerospace systems is very limited. By their nature, high-order methods are not as mathematically compact as low-order methods and thereby require many more base (nodal) points to interpolate within their stencil. This explains why the spectral method and p-type finite element schemes in their standard implementation cannot handle strong gradients of the dependent variables going from one nodal point to another. ENO and WENO avoid this problem by effectively using dependent variable values in the smooth regions adjacent to nodal points in the construction of the stencil. The stretched, curvilinear and deforming meshes, which are required for most practical aerospace systems, cause spurious oscillations when high-order schemes are used,[9] and thereby potentially limit their applicability. Moreover, when three-dimensional curvilinear meshes are employed, the use of standard metric evaluation procedures significantly degrades accuracy since free-stream preservation is violated. A remedy for this has been proposed.[9]

ENO and WENO schemes also have their own problems that could potentially undermine their applicability to realistic systems. For example, for ENO, there is sometimes the need to bias the procedure toward a locally-centered stencil, particularly when Mach number is low. Boundary treatments for WENO are also potential issues. Weirs and Candler[12] have proposed procedures to address the problem of excessive damping when the WENO procedure is used for direct numerical simulation (DNS).

Despite the potential advantages of high-order methods implied in the foregoing, it is still the case that the procedures have not been applied to complex aerospace systems. The present paper has the objective of addressing this issue by investigating realistic systems using high-order methods. What complicates this situation is the fact that one has to deal with the inherent problems of high-order methods within the context of other procedures that are needed in order to calculate flows in realistic geometries. For example, it is not clear how the overset procedure works for high-order calculations involving complex geometries that are meshed with highly-skewed curvilinear grids. This and other challenges of using high-order methods for complex geometries will be addressed in this paper.

The computational vehicle within which the present studies are carried out is the AEROFLO multidisciplinary CFD code, developed by Thaerocomp Technical Corporation. However, the present paper is non-commercial and serious research issues are addressed in connection with the use of high-order methods for Boeing 747-200 aircraft.

## II. The Basic Flow Equations

The fully compressible form of the continuity, momentum, and energy equations are employed in this study since we are interested in the nonlinear coupling between the acoustic and vorticity fields. Assuming large eddy simulation (LES), the Favre-averaged equations are written in a conservative form:

$$\frac{\partial \overline{\rho}}{\partial t} + \frac{\partial \left(\overline{\rho}\widetilde{u}_i\right)}{\partial x_i} = 0,$$

$$\frac{\partial \left(\overline{\rho}\widetilde{u}_i\right)}{\partial t} + \frac{\partial \left(\overline{\rho}\widetilde{u}_i\widetilde{u}_j + \overline{p}\delta_{ij}\right)}{\partial x_j} = \frac{\partial \left(\tau_{ij} - \tau_{ij}^{SGS}\right)}{\partial x_j},$$

$$\frac{\partial \left(\overline{\rho}\widetilde{E}\right)}{\partial t} + \frac{\partial \left(\left(\overline{\rho}\widetilde{E} + p\right)\widetilde{u}_j\right)}{\partial x_j} = \frac{\partial \left(\widetilde{u}_i\tau_{ij} - q_j + H_i^{SGS} + \sigma_j^{SGS}\right)}{\partial x_j}.$$

Here, $\overline{\rho}$ is the mass density, $\left(\widetilde{u},\widetilde{v},\widetilde{w}\right)$ are the velocity components along the physical coordinate directions ($x$,$y$,$z$), and $\widetilde{E}$ is the total specific energy. In LES, the large scale motion is fully resolved while the effect of the small scale structures is modeled. The separation between large and small scales is determined by the grid size, $\Delta$. In the system of transport equations shown above, the filtered viscous stress tensor, $\tau_{ij}$, and heat flux vector, $q_i$, are based on the filtered flow field values. The sub-grid scale (SGS) terms represent the effect of the small scale structures on the resolved scales:

$$\tau_{ij}^{SGS} = \overline{\rho u_i u_j} - \overline{\rho}\widetilde{u}_i\widetilde{u}_j, \quad \sigma_j^{SGS} = \overline{u_i\tau_{ij}} - \widetilde{u}_i\overline{\tau_{ij}},$$

$$H_i^{SGS} = \overline{\rho E u_i} - \overline{\rho}\widetilde{u}_i\widetilde{u}_j + \overline{pu_i} - \overline{p}\widetilde{u}_i.$$

The unclosed viscous work, $\sigma_j^{SGS}$, is assumed negligible and thus ignored in the present work. The SGS contribution to the shear stresses, $\tau_{ij}^{SGS}$, is computed using the Smagorinsky model:

$$\tau_{ij}^{SGS} = -2\nu_t\overline{\rho}\widetilde{S}_{ij} + \frac{2}{3}\overline{\rho}\left(\nu_t\widetilde{S}_{kk} + k^{SGS}\right)\delta_{ij},$$

where $\nu_t = C_R\left(D\Delta\right)^2\sqrt{2\widetilde{S}_{ij}\widetilde{S}_{ij}}$ is the eddy viscosity, $k^{SGS} = C_I\left(D\Delta\right)^2\sqrt{2\widetilde{S}_{ij}\widetilde{S}_{ij}}$ is the SGS kinetic energy, and $\widetilde{S}_{ij} = \frac{1}{2}\left(\frac{\partial\widetilde{u}_i}{\partial x_j} + \frac{\partial\widetilde{u}_j}{\partial x_i}\right)$ is the strain rate tensor. $C_R$ and $C_I$ are either constant, determined empirically, or are dynamically computed as a function of local flow conditions using the formulation of Germano and co-workers[13] and Moin et al.[14] with the modification proposed by Lilly.[15] For the simulations where $C_R$ and $C_I$ are constant, van-Driest damping function is used near solid walls: $D = 1 - \exp\left(-y^{+3}/26\right)$, where $y^+ = yu_\tau/\nu$, $y$ is the distance to the nearest wall, $u_\tau$ is the friction velocity, and ν is the kinematic viscosity.

The SGS energy flux, $H_i^{SGS}$, is modeled as

$$H_i^{SGS} = -\overline{\rho}\frac{\nu_t}{\mathrm{Pr}_t}\left(\frac{\partial\widetilde{h}}{\partial x_i} + \widetilde{u}_j\frac{\partial\widetilde{u}_j}{\partial x_i} + \frac{1}{2}\frac{\partial k^{SGS}}{\partial x_i}\right). \tag{4}$$

Here, $\widetilde{h}$ is the filtered specific enthalpy. The turbulent Prandtl number, $Pr_t$, can be either considered constant or be dynamically computed during the simulation.

The filtered total specific energy is given as

$$\widetilde{E} = \int_{T_0}^{\widetilde{T}} c_p\,dT - \frac{\overline{p}}{\overline{\rho}} + \frac{\widetilde{u}_i\widetilde{u}_i}{2} + k^{SGS}. \tag{5}$$

In order to facilitate the numerical simulation of flow configurations in, or over, arbitrary complicated bodies, the transport equations need to be re-cast for a generalized curvilinear coordinate system. In order to facilitate this conversion, the equations are written in vector form as

$$\frac{\partial Q}{\partial \tau}+\frac{\partial F}{\partial x}+\frac{\partial G}{\partial y}+\frac{\partial H}{\partial z}=\frac{\partial F_v}{\partial x}+\frac{\partial G_v}{\partial y}+\frac{\partial H_v}{\partial z}+S\,, \tag{6}$$

where $Q$ is the vector of conserved variables, $Q=\left(\rho,\rho u,\rho v,\rho w,\rho E\right)^T$, $(F,G,H)$ are the convective fluxes, $(F_v,G_v,H_v)$ are the viscous fluxes, and $S$ is the source term, which is non-zero only in the energy equation. In a curvilinear coordinate system $(\xi,\eta,\zeta)$, the transport equations (6) are written as

$$\frac{\partial\left(Q/J\right)}{\partial t}+\frac{\partial \hat{F}}{\partial \xi}+\frac{\partial \hat{G}}{\partial \eta}+\frac{\partial \hat{H}}{\partial \zeta}=\frac{\partial \hat{F}_v}{\partial \xi}+\frac{\partial \hat{G}_v}{\partial \eta}+\frac{\partial \hat{H}_v}{\partial \zeta}+\hat{S}\,, \tag{7}$$

where $J$ is the Jacobian of the transformation between the generalized coordinate system $(\xi,\eta,\zeta)$ and physical coordinate system $(x,y,z)$. The convective flux in the computational $\xi$-direction is given by

$$\hat{F}=\frac{1}{J}\left(\xi_x F+\xi_y G+\xi_z H\right). \tag{8}$$

The expressions for the other convective and viscous fluxes are similar. The transformed source term is computed as $\hat{S}=S/J$.

### A. The Turbulence Models

The simplest turbulence models in AEROFLO are the one-equation Spalart-Allmaras[16] and the detached eddy simulation (DES)[17] models. Also supported are several two-equation turbulence models, namely the standard Launder-Sharma k-ε model, Abid k-ε model, and Menter's SST (Shear-Stress-Transport) k-ω model.[18] The LES procedure, although the choice for accurate calculation of massively separated flows, is too expensive in its present form. Cost was the motivation for the development of DES. However, DES is grid-dependent, like LES. We are interested in establishing a unified, if not automatic, grid-independent approach that moves from RANS towards LES. To that end, we are investigating and further developing the partially-resolved numerical simulation (PRNS) approach.[19,20] The various turbulence models in our procedure use one form of eddy-viscosity model or another:

$$\tilde{\tau}_{ij}^{\,T}=2\tilde{\mu}_T\left(\tilde{S}_{ij}-\frac{1}{3}\frac{\partial \tilde{u}_k}{\partial \tilde{x}_k}\delta_{ij}\right)-\frac{2}{3}\tilde{\rho}\tilde{k}\delta_{ij}\,,$$

where $\tilde{k}$ is the turbulent kinetic energy which is equal to $\frac{1}{2}(u'^2+v'^2+w'^2)$. Note that in the calculation of certain non-reacting flows in AEROFLO, $\tilde{k}$ is ignored in the definition of the total energy, $\tilde{E}$, on the assumption that $\tilde{k}<<\tilde{e}+\frac{1}{2}\left(\tilde{u}^2+\tilde{v}^2+\tilde{w}^2\right)$. The turbulent viscosity $\tilde{\mu}_t$ is modeled by one of the several methods mentioned above. For more details, please consult the original papers. The scalar equations, including those associated with the turbulence models (viscosity, kinetic energy and its dissipation rate, vorticity $\omega$ in the $k-\omega$ equation, etc.) are written in the form

$$\frac{\partial \phi}{\partial t}+U\frac{\partial \phi}{\partial \xi}+V\frac{\partial \phi}{\partial \eta}+W\frac{\partial \phi}{\partial \zeta}=\frac{J}{\rho}\cdot\frac{\partial}{\partial \xi}\left[\left(\mu+\frac{\mu_t}{\sigma_\phi}\right)\frac{\xi_{,i}}{J}\left(\xi_{,i}\frac{\partial \phi}{\partial \xi}+\eta_{,i}\frac{\partial \phi}{\partial \eta}+\zeta_{,i}\frac{\partial \phi}{\partial \zeta}\right)\right]$$

$$+\frac{J}{\rho}\cdot\frac{\partial}{\partial \eta}\left[\left(\mu+\frac{\mu_t}{\sigma_\phi}\right)\frac{\eta_{,i}}{J}\left(\xi_{,i}\frac{\partial \phi}{\partial \xi}+\eta_{,i}\frac{\partial \phi}{\partial \eta}+\zeta_{,i}\frac{\partial \phi}{\partial \zeta}\right)\right]$$

$$+\frac{J}{\rho}\cdot\frac{\partial}{\partial \zeta}\left[\left(\mu+\frac{\mu_t}{\sigma_\phi}\right)\frac{\zeta_{,i}}{J}\left(\xi_{,i}\frac{\partial \phi}{\partial \xi}+\eta_{,i}\frac{\partial \phi}{\partial \eta}+\zeta_{,i}\frac{\partial \phi}{\partial \zeta}\right)\right]+P+D,$$

where $(\,)_{,i}$ implies $\partial/\partial x_i$ of the quantity ( ), and $P$ and $D$ are the production and destruction terms, respectively.

## III. The Defining Numerical Schemes in AEROFLO

### A. The Spatial Schemes

The spatial schemes in the high-order procedures presented are based on the finite difference method, because of the low cost relative to other options, such as finite volume and finite elements. Shu[7] suggested that the finite volume method is approximately nine times as expensive. The finite element method could even be more expensive because of the numerical quadrature that is required for high-order schemes. We investigate the MUSCL schemes for low-order calculations and the compact and WENO schemes for high-order discretization. The compact scheme is intended for incompressible and subsonic flows, whereas WENO is used for transonic and supersonic flows. The basic forms of the schemes are summarized below.

*1. MUSCL*

This simple, fairly robust, low-order scheme that uses Roe flux-splitting at the mid-point values was introduced by van Leer. First, the left and right values of the primitive variables at mid-point between two nodes are computed as

$$\phi_{i+1/2,L} = \phi_i + \beta_i \quad \text{and}$$
$$\phi_{i+1/2,R} = \phi_{i+1} - \beta_{i+1}$$

where $\phi = (\rho,u,v,w,p)^{\mathrm{T}}$ is the vector of primitive variables and $\beta_i$ is the "limited slope" at point $i$. Here, $p$ is the thermodynamic pressure. The limited slopes $\beta_i$ are computed using van Leer's harmonic limiter.

Based on the left and right states at *i+1/2*, the numerical flux is computed using Roe flux-splitting as

$$\hat{F}_{i+1/2} = \frac{1}{2}\left( \hat{F}_{i+1/2,L} + \hat{F}_{i+1/2,R} - |A|\left(\left(\frac{Q}{J}\right)_R - \left(\frac{Q}{J}\right)_L\right)\right).$$

Here, "*R*" and "*L*" values are constructed using the corresponding values of the primitive variables in equation (6). Matrix $|A|$ is constructed using the Roe-averaged state at *i+1/2*:

$$|A| = R_{Roe}|\Lambda_{Roe}|R_{Roe}^{-1},$$

where $|\Lambda|$ is the diagonal matrix of the absolute eigenvalues of the Jacobian, $\partial\hat{F}/\partial Q$.

*2. Compact*

The Padé method is used to approximate the spatial derivatives for subsonic flows. Consider the differencing of a variable $\phi$ (e.g. a conserved variable, a flux component, etc.) along the $\xi$ direction, or $\phi' = \partial\phi/\partial\xi$. An implicit, centered finite difference formula is employed to calculate the numerical values $\phi_i'$:

$$\alpha\phi_{i-1}' + \phi_i' + \alpha\phi_{i+1}' = b\frac{\phi_{i+2} - \phi_{i-2}}{4\Delta\xi} + a\frac{\phi_{i+1} - \phi_{i-1}}{2\Delta\xi}.$$

The parameters $\alpha$, $a$, and $b$ determine the spatial accuracy of the algorithm. Their values are determined from a Taylor series expansion around point *i*. For a sixth-order accurate scheme,[2,8] $(\alpha,a,b) = \left(1/3, 14/9, 1/9\right)$.

Compact finite differences are non-dissipative and are therefore susceptible to the numerical instabilities that are due to flow nonlinearities. In order to enforce numerical stability, a low-pass filtering procedure is adopted. For a typical component of the solution vector, $\phi$, the filtered values $\tilde{\phi}$ are obtained from

$$\alpha_f\tilde{\phi}_{i-1} + \tilde{\phi}_i + \alpha_f\tilde{\phi}_{i+1} = \sum_{k=0}^{N}\frac{a_k}{2}\left(\phi_{i+k} + \phi_{i-k}\right).$$

The coefficients $a_k$ are expressed in terms of the parameter $\alpha_f$,[8] which controls the strength of the filter, and as it is reduced, a wider band of high frequencies is damped. A range $0.3 \le \alpha_f < 0.5$ is suggested.

*3. WENO*

For high-order differencing of flow fields with shock waves, the characteristic-wise WENO procedure is used (see Ref. [7], procedure 2.10). This numerical approach is summarized below.

Considering the $\xi$-direction as an example, we have

$$\left.\frac{\partial \hat{F}}{\partial \xi}\right|_i = \frac{1}{\Delta\xi}\left\{\left[\widetilde{R}_{Roe}\cdot\left(\widetilde{R}_{Roe}^{-1}\cdot\hat{F}\right)\right]_{i+1/2} - \left[\widetilde{R}_{Roe}\cdot\left(\widetilde{R}_{Roe}^{-1}\cdot\hat{F}\right)\right]_{i-1/2}\right\},$$

where $\widetilde{R}_{Roe}$ is the matrix formed with the right eigenvectors of the Jacobian $\partial\hat{F}/\partial Q$ computed based on a Roe-averaged state at *i±1/2*. For the characteristic-wise WENO, the reconstruction procedure is performed on the characteristic fields $\hat{F}_c = \widetilde{R}_{Roe}^{-1}\cdot\hat{F}$ to obtain the values at *i+1/2*. The Lax-Friedrichs flux-splitting method is used to obtain the left and right states at the mid-points:

$$\hat{F}_c^{\pm} = \frac{1}{2}\left(\hat{F}_c \pm \alpha q\right),$$

where $\alpha$ is the spectral radius of the Jacobian $\partial\hat{F}/\partial Q$. The characteristic-wise fluxes at the mid-points are reconstructed as

$$\hat{F}^{+}_{c,i+1/2} = \sum_{r=0}^{k-1}\omega_r F^{(r)+}_{c,i+1/2},\quad \hat{F}^{-}_{c,i+1/2} = \sum_{r=0}^{k-1}\widetilde{\omega}_r F^{(r)-}_{c,i+1/2},\quad F^{(r)}_{c,i+1/2} = \sum_{m=0}^{k-1} c_{rm}\hat{F}_{c,i-r+m}\ ,$$

where $\omega_r$ and $\widetilde{\omega}_r$ are normalized weights, based on smoothness indicators of the numerical fluxes and $c_{rm}$ are the coefficients for Lagrange interpolation.[7] Finally, the reconstructed characteristic fluxes are converted back to physical space, $\hat{F}^{\pm}_{i+1/2} = \widetilde{R}_{Roe}\cdot\hat{F}^{\pm}_{c,i+1/2}$, and the numerical flux formed as

$$\hat{F}_{i+1/2} = \hat{F}^{+}_{i+1/2} + \hat{F}^{-}_{i+1/2}.$$

The viscous fluxes are discretized with explicit second-order finite differences when the MUSCL scheme is used for the convective fluxes, and with high-order finite differences when the compact (sixth-order) or WENO (fifth-order) schemes are used for the convective fluxes.

**B. Time Integration**

Several time-marching schemes are supported in AEROFLO. For problems where accurate time-dependent solutions are required, the classical fourth-order Runge-Kutta (RK4) scheme is employed in its low-storage form. Because of its relatively severe stability constraint, RK4 is inappropriate for flow problems in which only the steady state solutions are sought. The approximate factorization procedure of Beam and Warming, with the diagonalized simplification by Pulliam and Chaussee,[21] is employed for these cases:

$$\begin{aligned}
&\left[\left(J^{-1}\right)^{(p+1)} + \frac{1}{1+\varphi}dt\delta_\xi\left(\frac{\partial\hat{F}^{(p)}}{\partial Q} - \frac{\partial\hat{F}_v^{(p)}}{\partial Q}\right)\right]J^{(p+1)}\times\\
&\left[\left(J^{-1}\right)^{(p+1)} + \frac{1}{1+\varphi}dt\delta_\eta\left(\frac{\partial\hat{G}^{(p)}}{\partial Q} - \frac{\partial\hat{G}_v^{(p)}}{\partial Q}\right)\right]J^{(p+1)}\times\\
&\left[\left(J^{-1}\right)^{(p+1)} + \frac{1}{1+\varphi}dt\delta_\zeta\left(\frac{\partial\hat{H}^{(p)}}{\partial Q} - \frac{\partial\hat{H}_v^{(p)}}{\partial Q}\right)\right]\Delta Q\\
&= -\frac{dt}{1+\varphi}\left[\begin{array}{l}\left(J^{-1}\right)^{(p+1)}\dfrac{(1+\varphi)Q^{(p)} - (1+2\varphi)Q^{(n)} + \varphi Q^{(n-1)}}{dt} +\\ \delta_\xi\left(\hat{F}^{(p)} - \hat{F}_v^{(p)}\right) + \delta_\xi\left(\hat{G}^{(p)} - \hat{G}_v^{(p)}\right) + \delta_\zeta\left(\hat{H}^{(p)} - \hat{H}_v^{(p)}\right)\end{array}\right]
\end{aligned},$$

where $\varphi = 1/2$ yields a three-point backward stencil in time. Here, derivatives $\delta_i$ are obtained with standard second-order centered differences in the implicit operators on the left-hand side, while the right-hand side differences are computed using the high- and low-order spatial schemes described above. In order to reduce the errors associated with the approximate factorization and diagonalization procedures, Newton-like sub-iterations are performed. Note that in the equation above, a superscript "*n*" denotes the iteration number, and superscript "*p*", the sub-iteration count. Within one iteration, $Q^{(p)} = Q^{(n)}$ and, at convergence in *p*, $Q^{(n+1)} = Q^{(p)}$. Typically three sub-iterations are applied per time step. Our code also supports a third-order total-variation-diminishing (TVD) Runge-Kutta time integration procedure.

## IV. The Challenges of High-Order Simulation in Complex Geometries

In this section, we discuss the difficulties encountered in our implementation and validation of the high-order schemes for complex aerospace geometries. A few of the problems exist for low-order schemes as well, but they are more serious for high-order schemes. These challenges are illustrated below.

### A. Generation of Overlapped Grid

Overlapping of the blocks in a multi-block grid system is a feature of AEROFLO. For high-order methods, a minimum of three nodal points is required in the overlap, whereas one nodal point is sufficient for low-order (second-order) schemes. This is illustrated in Fig. 1(b) for an airfoil/flap configuration, where the required three overset nodes are shown at the interface between the blocks. Fig. 1(a) shows only one overset node that is required for low-order schemes in a curvilinear coordinate direction at the overlap boundary. The high-order requirement at an overlap boundary remains independent of how the boundaries are generated. In Fig. 1, the boundaries result from an overset "hole-cut." This requirement implies that a minimum of seven nodal points are needed in a given direction in a block, since three nodal points in that direction will receive their solutions from the adjacent block while three other nodal points (in the block) are needed to donate solutions to an adjacent block. This requirement is one of the reasons why mesh generation is relatively more complicated for high-order methods. (Note that the term "overset nodes" is used in this paper to refer to nodal points in a block that receive their solutions from an adjacent block.)

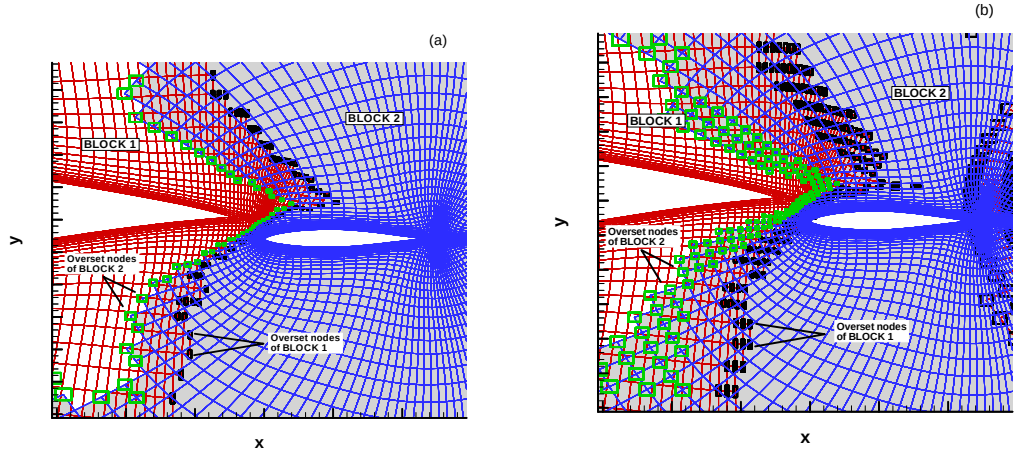


Figure 1 Overset boundary in an airfoil/flap configuration:
(a) Low-order overlap, (b) High-order overlap

### B. Stricter Mesh Quality Requirement

Compared to low-order methods, high-order procedures are particularly affected by poor mesh quality. The high-order schemes used in AEROFLO perform best, in terms of maintaining their accuracy and stability, when the grid sizes in adjacent blocks are uniform. That is, the procedures require uniform grid spacing going from one block to another. The transformation metrices $\xi_x, \xi_y$, etc. become discontinuous otherwise, leading to potentially severe problems for high-order methods. (Note that the metrices have to be differentiated to high-order.)

In low-order simulations, the disparity in mesh sizes from adjacent blocks, as shown in Fig. 2, will be considered very acceptable. (In fact, we have carried out low-order simulations where the ratio of adjacent mesh sizes was greater than 500 (Ladeinde[22]).)

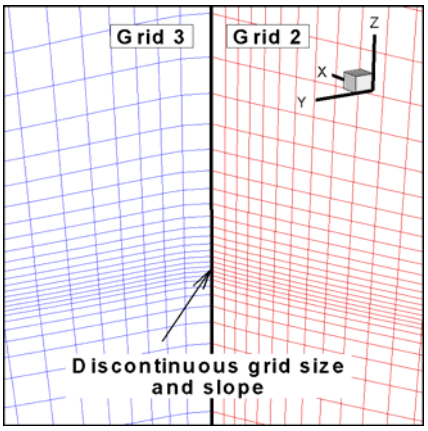


Figure 2 Details of the interface between two adjacent blocks from a 6-block conforming Boeing 747 grid.

Fig. 3 shows that the low-order MUSCL scheme was unruffled, whereas WENO reacted very badly. This is one advantage of the overset method, which allows physically-sound calculations in a region with a "bad" mesh, because a better quality mesh can be superimposed and successfully used in such regions.

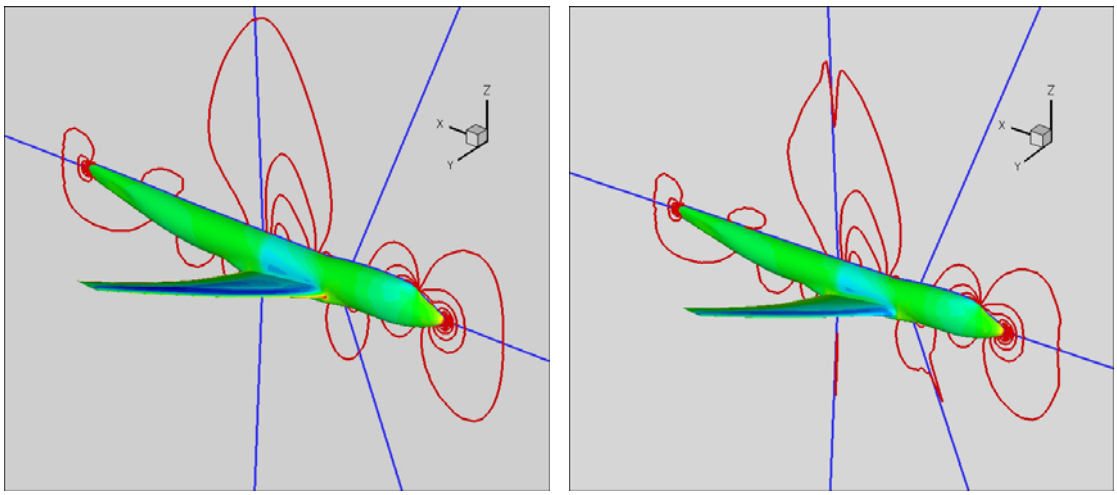

Figure 3 Pressure contours of calculations on grids with discontinuous grid spacing (a) MUSCL calculations, (b) WENO calculations. Note the unphysical pressure distribution at the interface between Grids 2 and 3 for WENO, which is due to the mesh size discontinuity in that region.

In principle, adaptive, ENO-style stencil selection process could be explored for differentiating the metrices, but this has not been pursued in our work because of other potential problems with this approach (such as free-stream preservation issues).

There are other grid-dependent demands from high-order differencing. The grids from the mesh generator sometimes come highly skewed for complex geometries. Included angles that approach 180º are not uncommon, with incipient singularity when the metrices are evaluated via finite differences. Such a situation is depicted in Fig. 4 below in the nose cone of a model of the Boeing 747-200 commercial aircraft. Using finite volume–type procedures to evaluate the metrices helps to obviate singular Jacobians. However, such use of finite volume has to be localized, since the procedure is very expensive for high-order calculations.[7]

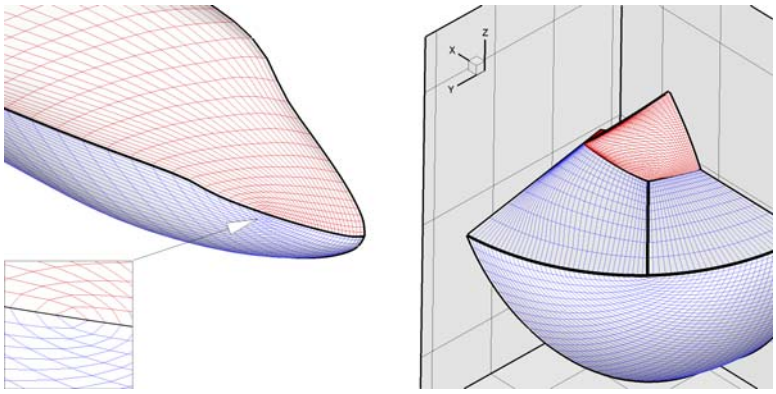

Figure 4 (a) Grid regions with singular Jacobians (b) Propagation of the problem region far into the computational domain.

An illustration of this problem using the two-dimensional schematics in Fig. 5 is presented below, with a C-C grid consisting of two blocks.

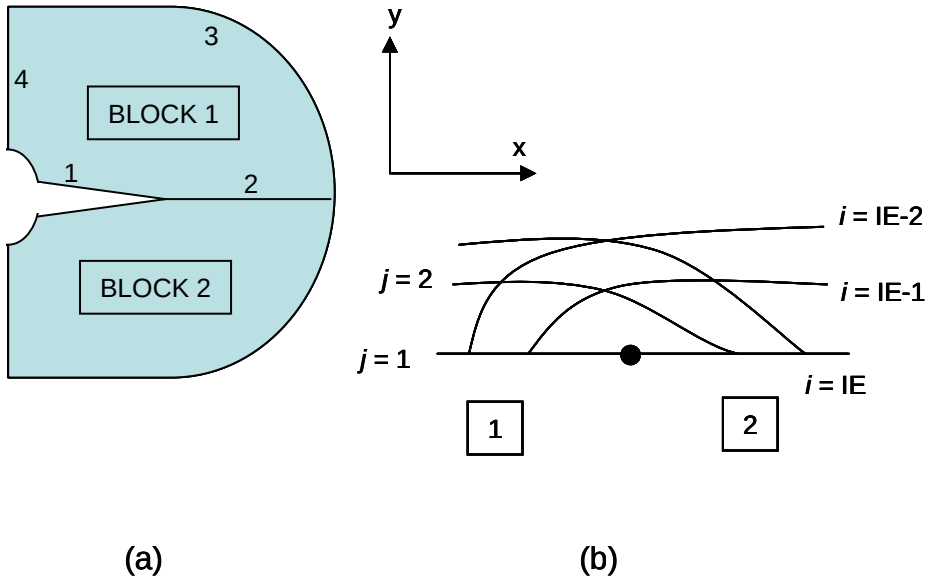


Figure 5 Illustration of degenerate Jacobian in a general schematic (a) Ensemble view of two adjacent blocks, (b) Close-up view of the C-C junction.

In this illustration, Block 1 is assumed to lie in the *k*-plane. Some of the coordinate derivatives at the point (shown as a dot in Fig. 5(b)) where Side 1 of Block 1 intersects with Side 2 of Block 1 are

$$y_\xi = y(IE,1,*) - y(IE-1,1,*) = 0.0,$$
$$y_\eta = y(IE,2,*) - y(IE,1,*) = 0.0,$$
$$y_\zeta = 0.0$$

Then the determinant of the Jacobian matrix:

$$\begin{vmatrix} x_\xi & y_\xi & z_\xi \\ x_\eta & y_\eta & z_\eta \\ x_\zeta & y_\zeta & z_\zeta \end{vmatrix}$$

will be zero at the point in question. (For the 3D problem, we will have zero Jacobians along the edge that passes though the point in Fig. 5(b).)

**C. WENO is Very "Shaky" at the Boundary**

Consider in Fig. 6 the five-point WENO stencil $x_k$, $i-2 \le k \le i+2,$ with the 3 sub-stencils $h_s$ $(s = 0,1,2).$ The computation of the fluxes at point *i* consists of a weighted stencil based on points *i-2* to *i+2*. At grid boundaries, such as in Fig. 6 (b), extra ghost nodes are required at *i-2*, and *i-1* in order to preserve the formulation. In our procedure, the values of the solution variables being differentiated at the ghost nodes are set infinitely large. This has the effect of minimizing the weightings associated with nodes i-2 and i-1, thereby resulting in a "second-order" stencil that (effectively) computes fluxes based only on points *i* through *i+2*.

The formulation is modified when the grid boundary in Fig. 6(b) is an overlap boundary. The modification is illustrated in Fig. 6(c) where the generated ghost nodes *i-2* and *i-1* are also designated as overset nodes that obtain interpolated values from neighboring grids. This modification is designed to maintain the high-order calculation of the fluxes at the boundaries.

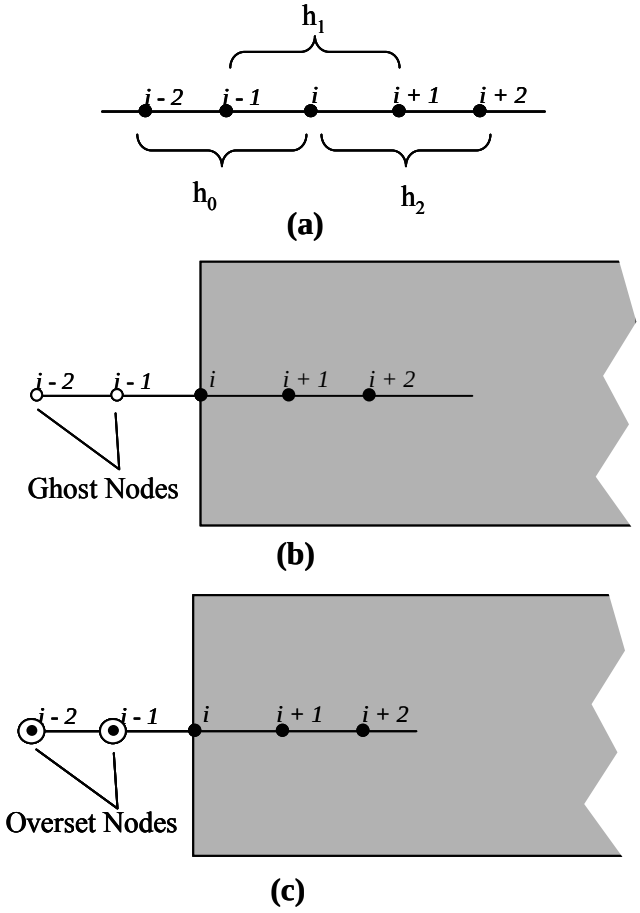


Figure 6 Illustration of boundary treatment for WENO

**D. Excessive Mesh Refinement Requirement**

This is a problem with conforming meshes. For example, the mesh needs to be substantially refined in order to capture the end effects at wing tips. With a conforming grid system, this refinement is propagated into regions where mesh refinement may not be required. This leads to unnecessary computational load, both in terms of the larger number of grid points and the need for a smaller time step size over a larger portion of the grid in a way that undermines the ability to take advantage of adaptive time-stepping in a reasonable portion of the domain.

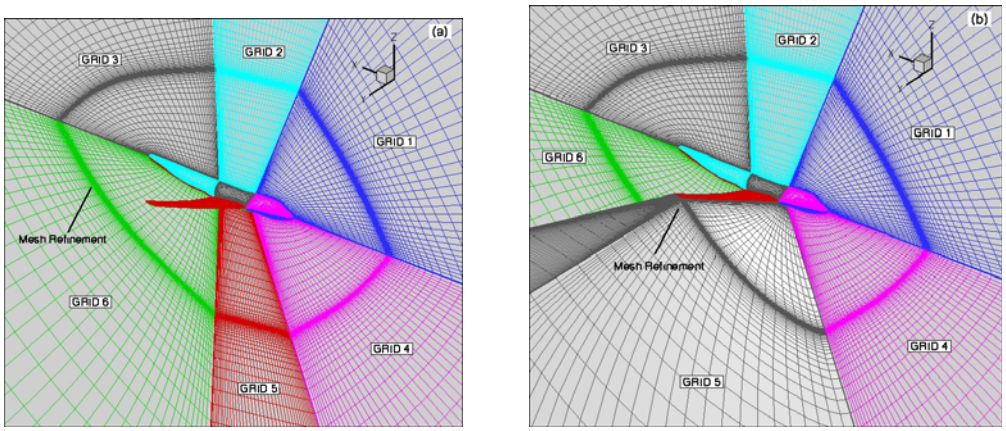


Figure 7 Excessive mesh refinement propagated globally for conforming grids
(a) Surface grids, (b) Surface grids and complete grid of block 5.

Fig. 7 illustrates this problem, where Fig. 7 (a) shows the surface grids around the fuselage of B747-200. The refinement (around the fuselage) is a result of wing tip refinement which is propagated to the other grids. Fig. 7 (b) shows the same grid but in which the complete block of grid 5 displayed to illustrate the source of the grid refinement observed in Fig. 7 (a). The solution to this is the use of an overset method.

Fig. 8 shows an overset grid around the same B747-200 plane. The figure focuses on the wing-body junction. The refinement at the end of the wing grid is not propagated to the fuselage grid, because an overset method with "hole-cut" is used. Therefore, the exchange of data between adjacent blocks does not require conforming grids at the interface.

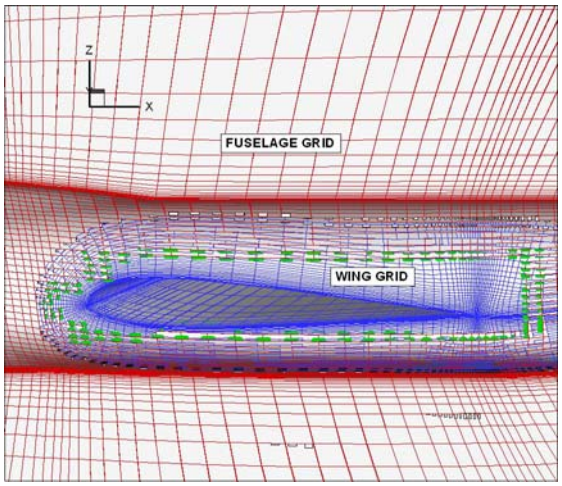


Figure 8 Overset grids around the B747 plane
focusing on the fuselage/wing junction.

### E. Filtering and Other Problems for the Overset Method

Despite the impression that the foregoing information may create, the overset method is not a cure-all. Within the framework of a high-order filtering procedure, there might not be a sufficient number of nodal points to perform a hole-cut. (Low-order methods will not suffer as much.) After a hole-cut, we could end up with too few number of nodal points (in a direction) between the natural boundary and the hole cut, which are not sufficient for high-order differencing. This is illustrated in Fig. 9 below for a two-block system used for the computation of flow over a V-gutter, which is a flame holder for the augmentor (after burner) of a high performance military plane. Block 2 contains the solid object and causes a "blanking" or hole-cut of sections of Block 1 using the overset method. The

hole-cut of Block 1 results in sections of the grid that do not contain a sufficient number of points for a high-order formulation.

The grids had to be regenerated in this case. Another difficulty with the overset method is that the interpolation errors between overset grids increase with the disparity in the sizes of the cells exchanging data. An incremental overset might be one way out, whereby blocks are progressively coarsened as we move away from the region requiring a fine grid.

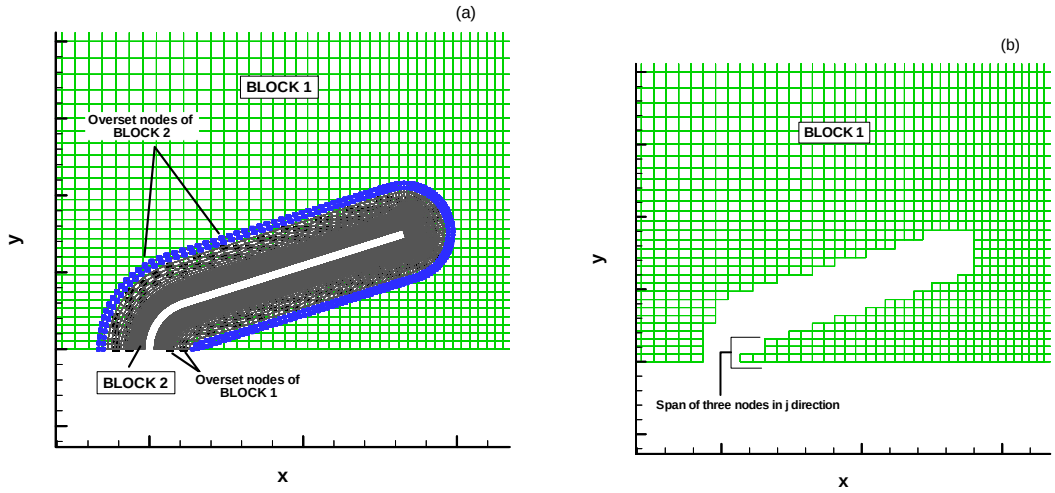


Figure 9 Degeneration of high-order formulation to low-order one
(a) Grids and overset nodes (b) Grid of block 1 alone.

## V. The Opportunities in High-Order Simulation in Complex Geometries

After our successful resolution (in the AEROFLO code) of the challenges discussed in the previous section, we are now ready to present the potential opportunities that come with high-order methods. The authors envision a situation whereby, in some really complex geometries, the relatively inefficient generation of structured mesh, vis-à-vis the extra demands by high-order schemes, could force a localized use of high-order schemes, rather than their use everywhere in the computational domain. Regions with very rich flow features (vortex shedding, massive separation, sound generation, etc.) could be solved with high-order methods, whereas a low-order procedure might be sufficient in the remaining parts of the solution domain. Nevertheless, the reader should be aware that the discussions presented in this section are based on the use of high-order or low-order methods everywhere in the computational domain, as the two approaches are not combined in this work. (The implementation of the hybrid procedure is presently being undertaken at Thaerocomp Technical Corporation.)

To establish the accuracy features of high-order methods and therefore their potentials, we report on the two important problems of turbulent flow over a backward-facing step (Steffen[23] and Driver and Seegmiller[24]) and flow over the ONERA M6 wing (Schmitt and Charpin[25]). These problems have been chosen because of their relevance to aerospace flow system simulation and the availability of experimental and simulation data for comparison. For the ONERA M6 wing, we will discuss the possibility of using much fewer grid points for the high-order calculations. Finally, we will summarize the high-order calculation of the flow over Boeing 747-200 commercial aircraft. Please note that all calculations with the high-order schemes exhibit grid-independence and show residuals that are characteristic of convergence. More details are provided below.

### B. Backward-Facing Step Calculations

The purpose of the calculation of the backward-facing step was to validate the high-order procedures and demonstrate the higher accuracy over low-order methods when the same flow parameters and computational grids are used. The conditions for the simulations of the backward-facing step problem were taken from Steffen[23] and NPARC website (Anonymous[26]). The schematic is shown in Fig. 10 below.

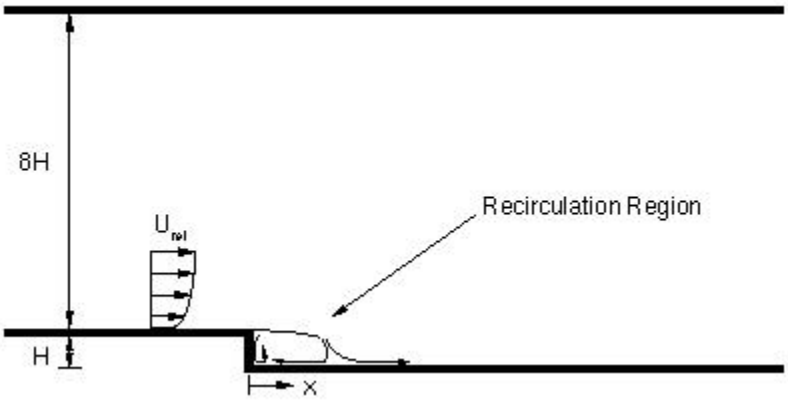

Figure 10 Backward-facing step configuration

The step height H is 0.5 inches. The grid consists of three blocks with a height prior to the step of *8H*. The inlet region prior to the step was set rather long (105H) (Fig. 11) in order to allow the turbulence to develop prior to separation at the step. A length of 50H is used after the step. The first block goes from -105H to 0 in *x*- and 1H to 9H in *y*. The second block goes from 0H to 50H in *x* and 1H to 9H in *y*, while the third consists 0H to 50H in *x*- and 0H to 1H in *y*. The three blocks consist of sizes 101 x 131, 138 x 131, and 138 x 55, respectively. The resolution is the same as in the WIND calculations, although it should be realized that, unlike in our model, the $238 \times 185$ grid used for the WIND calculations include the region $(x, y) \in (-105H, 0H) \times (0H, 1H)$. Thus, our grid has $101 \times 55 = 5{,}555$ nodal points fewer than WIND's. The same grid is used in the flow region in both codes.

In terms of the boundary conditions, no-slip conditions are applied on the bottom and top walls, except at the first 12 grid points at the top wall close to the inlet region, where a slip condition was imposed. An inlet condition of $U_{ref}$ = 44.2 m/s is applied and no-stress conditions are specified at the outflow. The fluid properties were obtained from the database in Thaerocomp's INSTED® thermal analysis software: $M_\infty$ = 0.128, $P_{ref}$ = 13.47psi = 92872.4Pa, $T_{ref}$ =534.16R = 296.756K, $\rho_{ref}$ = 1.176536kg/m$^3$, $\mu_{ref}$ = 1.82978 x 10-5 Ns/m$^2$. The Reynolds number based on the step height is *Re* = 35961.8.

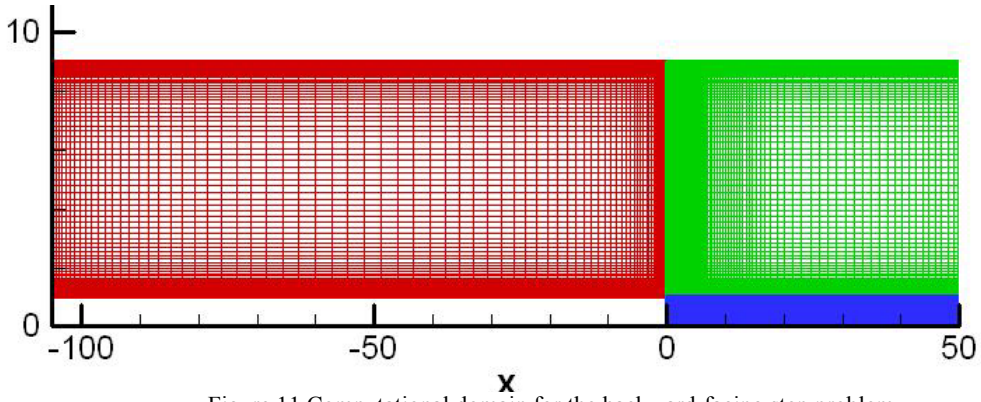

Figure 11 Computational domain for the backward-facing step problem

Calculations were carried out using the compact (high-order) and MUSCL (low-order) schemes in AEROFLO. The Spalart-Allmaras and Abid's *k-ε* turbulence models were evaluated. The calculations were compared to experimental measurements reported by Driver and Seegmiller[24] and the results from WIND calculations (Anonymous[26]). Fig. 12 compares the mean flow profiles obtained from the compact and MUSCL schemes in AEROFLO. The Spalart-Allmaras turbulence model is used for these calculations. It is evident that the results from the compact scheme are more accurate than those obtained with MUSCL. Figs. 13 and 14, respectively, compare the mean velocity and Reynolds stress profiles from AEROFLO and WIND, using the same *k-ε* turbulence model. Note that WIND uses the finite volume method with Roe upwind or Coakley upwind for stretched grids. (The procedures

used in AEROFLO have been summarized earlier in this paper.) It can be seen that both codes performed very well on the average velocity and that the compact results are slightly better. The compact results in AEROFLO are also visibly more accurate than the WIND results for the Reynolds stress. The $C_p$ distribution at the bottom and top walls of the channel are also accurately predicted by the compact schemes in AEROFLO (Fig 15).

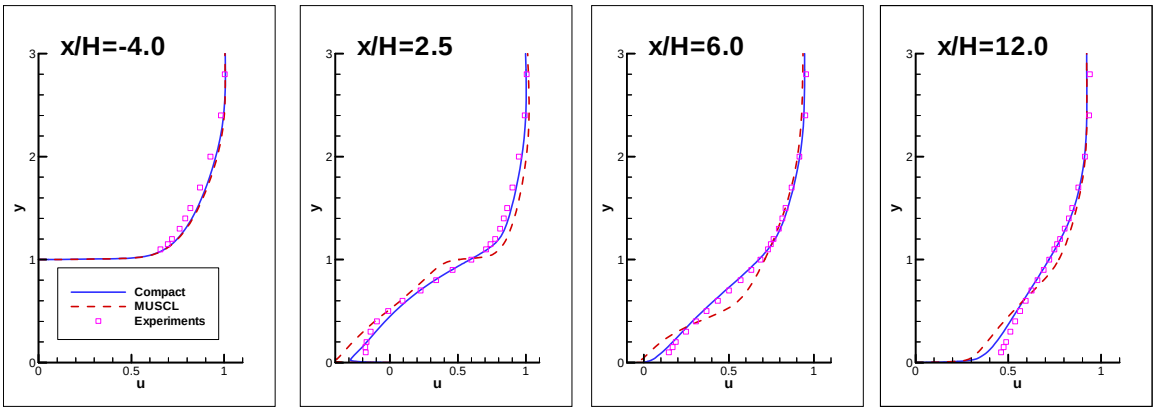


Figure 12 Mean velocity profile computed by compact and MUSCL schemes
in AEROFLO. The Spalart-Allmaras turbulence model was used.

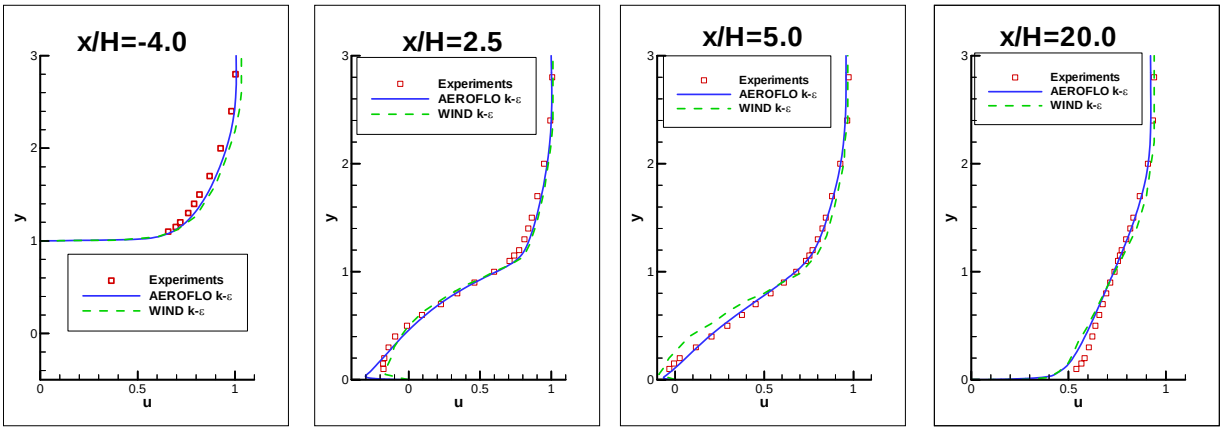


Figure 13 Mean velocity profiles obtained with the compact schemes
in AEROFLO and from WIND, using the $k$-$\varepsilon$ turbulence model

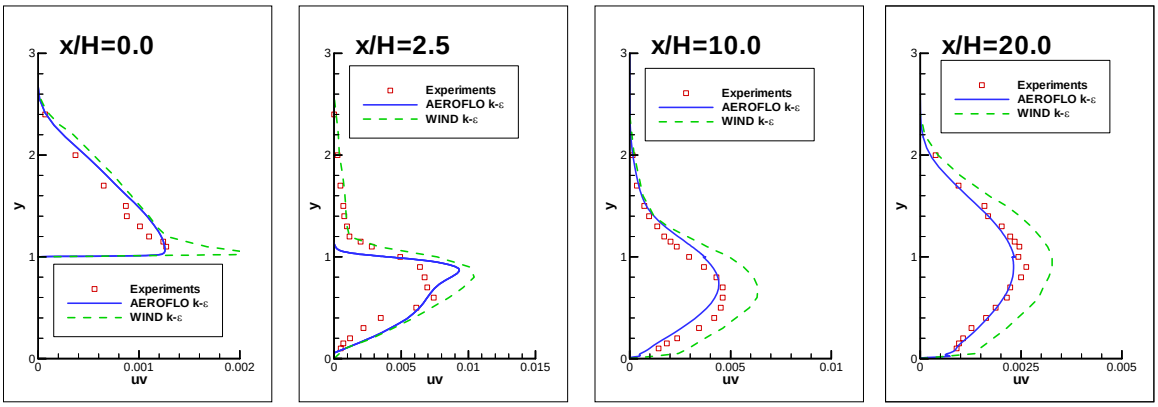


Figure 14 Reynolds stress profiles obtained with the compact schemes

in AEROFLO and from WIND, using the $k$-$\varepsilon$ turbulence model

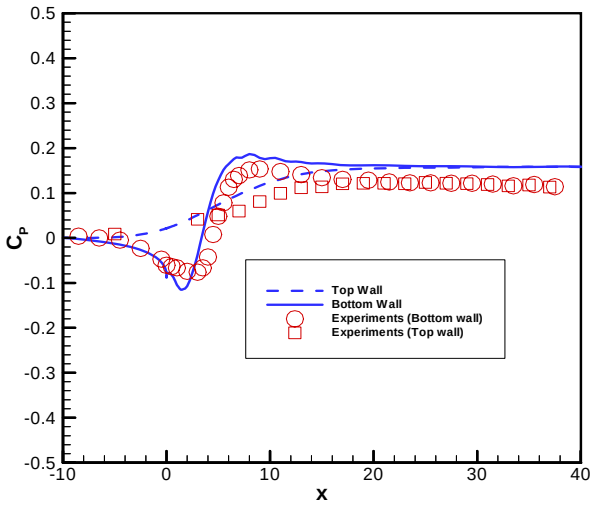


Figure 15 $C_p$ profile obtained from the compact schemes in AEROFLO.

**B. Flow Past the ONERA M6 Wing**

The purpose of the calculation of the ONERA M6 wing was to validate our high-order method for a geometry that is more realistic that the backward-facing step and for which a database exists for comparison. For the present task, we first validate our low-order MUSCL scheme by comparing the inviscid results with those in Jameson[27] for the coefficient of pressure. A single block with $189 \times 40 \times 50$ or 378,000 grid points was used for this case. It is an O-grid in which the $i$-direction is oriented along the surface of the wing, $j$ normal to the surface, and $k$ along the wing span. The problem was solved with the "far-field" assumption at the wing tip. Slip conditions were applied at both the wing surfaces and the wing-body interface at $k = 1$. The flow features are shown in the pressure contours of Fig. 16, in which the distribution of $C_p$ along the $x$-direction at various stations along $z$ with $j = 1$ are compared with calculations by Jameson in Fig. 17. Note the close agreement.

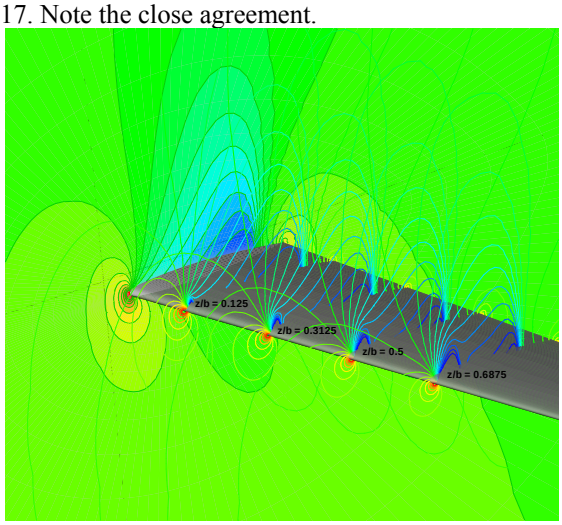


Figure 16 AEROFLO pressure results for the ONERA M6 wing using the MUSCL scheme.

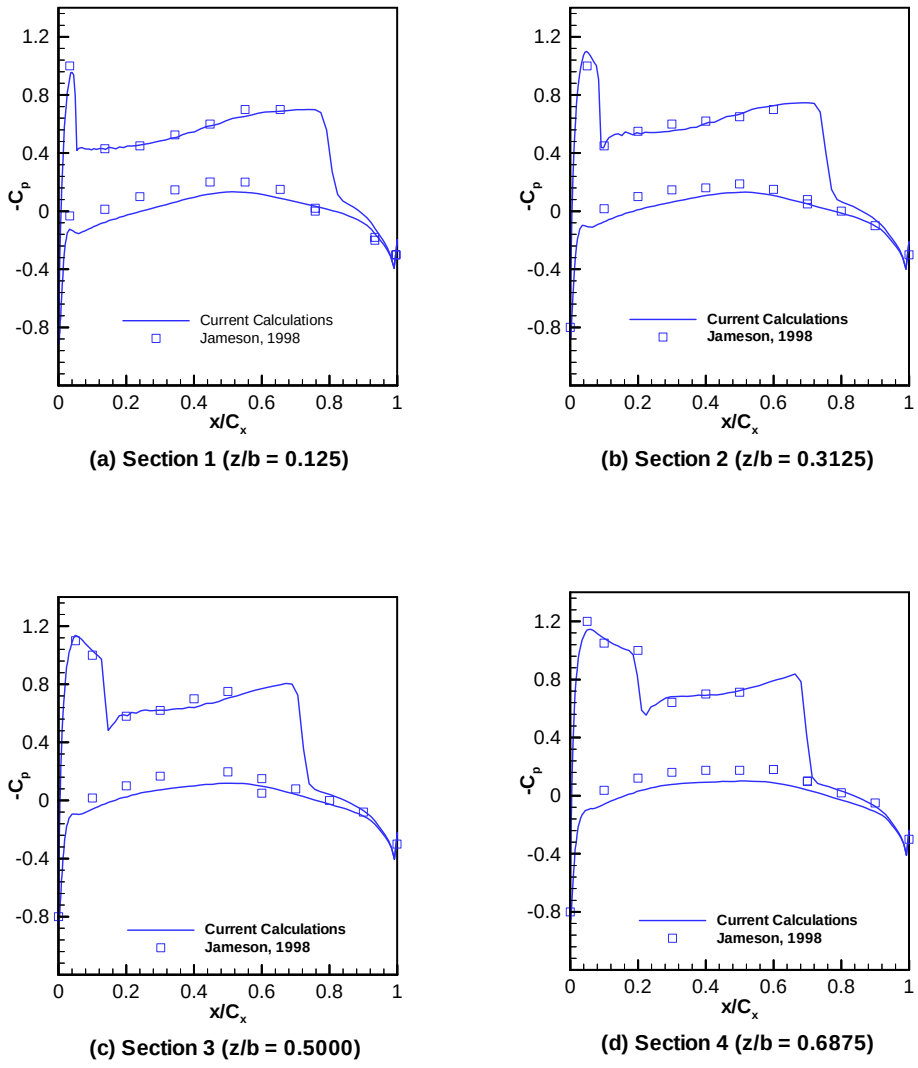


Figure 17 Pressure results for the ONERA M6 wing obtained with the MUSCL scheme in AEROFLO, showing comparison with the calculations of Jameson.[27]

Next, we carried out full three-dimensional calculations with both the MUSCL and WENO schemes in AEROFLO and compared these to results from WIND and experimental measurements. The 3-block Euler grid used in AEROFLO is a combination of two large H-H grids, for the upper and lower sides of the wing, respectively, and a smaller C-type grid for a better solution near the leading edge of the wing: upper side of wing (99×57×33=182457), lower side of wing (99×57×33=182457), and leading edge patch (41×45×22=40590). This gives a total of 413,000 grid points. The normal grid space near the wing is $5\times10^{-3}$. A view of the mesh is shown in Figure 18.

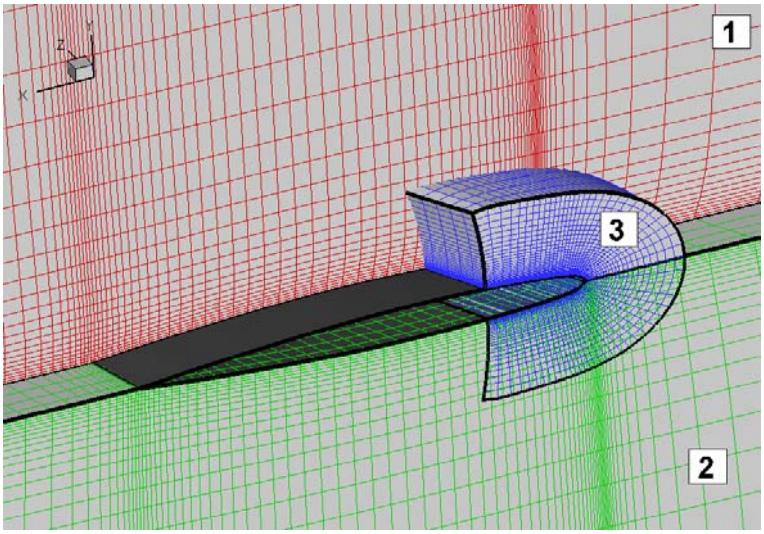


Figure 18 The computational grid around the ONERA wing. Certain (x-y) planes from Block 1 were "blanked out" to enhance the visualization of the overlap with Block 3.

Note that the mesh used on the surface of the wing consists of (50×33) (AEROFLO) and (79×33) (WIND) nodal points. These are shown in Figure 19.

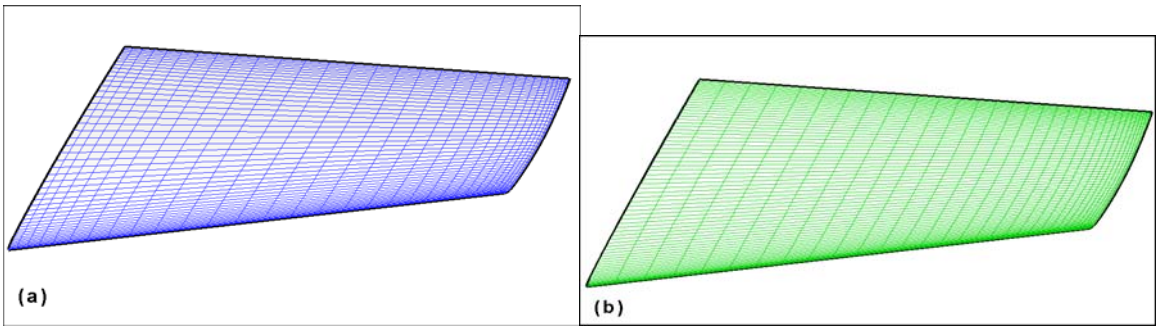


Figure 19 Comparison of the ONERA M6 surface grid used by (a) AEROFLO (50×33) grid points and (b) WIND (79×33) grid points.

In the experiments (Schmitt and Charpin, 1979), the Reynolds number was $\mathrm{Re} = 11.72 \times 10^6$, the Mach number $M_\infty = 0.8395$, and the angle of attack $\alpha = 3.06^\circ$. The gradient of pressure is zero while the density and velocities are prescribed at the inflow. The streamwise and transverse velocity components are set to match the reference Mach number and angle of attack. At all other external boundaries, zero-gradient conditions are prescribed for all variables, except the pressure, which is imposed at the outlet. The interface between Blocks 1 and 2 conform, which allows a natural extension of the computational scheme across this boundary without the loss accuracy. Slip wall conditions are imposed at the wing surface. The converged results are shown in Fig. 20, where we compare high-order calculations with low-order, WIND, and experimental results. It can be observed that both WIND and AEROFLO (WENO) results are quite accurate; the MUSCL results are not completely bad but they are certainly inferior by comparison. Note that MUSCL and WENO use 1650 surface grid points, whereas WIND uses 2409. It is also emphasized that no difficulties were encountered in getting the high-order calculations to converge. This supports the assertion that high-order schemes require fewer nodal points, even for non-canonical problems.

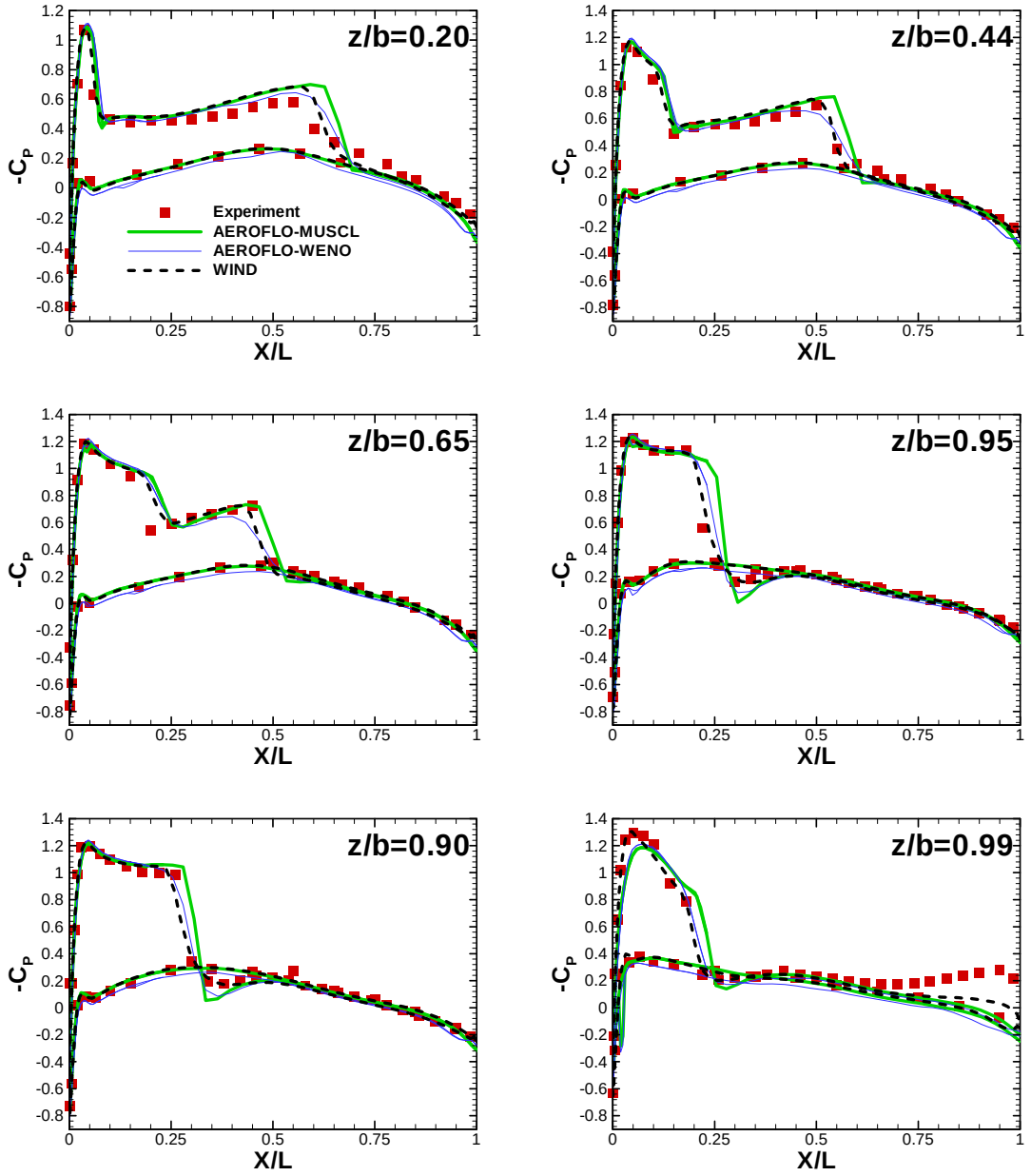


Figure 20 The measured and calculated profiles for the pressure coefficient. MUSCL and WENO are, respectively, low-order and high-order schemes in AEROFLO. "WIND" is a high-fidelity code developed by the NPARC Alliance. Experimental data points correspond to those of Schmitt and Charpin.[25]

### C. Calculation of Flow over Boeing 747-200 Commercial Aircraft

The purpose of the simulation in this section was to demonstrate the feasibility of calculating a realistic airframe with the high-order procedure presented in this paper. To our knowledge, no previous work has been able to carry out this kind of calculation. The reasons for this might be associated with the challenges discussed in the previous section of the paper.

The following conditions were used: $M_\infty = 0.855$, $\alpha$ = 3.05, reference area = 5500 sq ft (792,000 sq in), moment Center = (1339.91, 0., 191.87) in., moment reference length = 327.8 in., and Re = 10680 per in. The spatial dimensions have been normalized with the moment reference length, leading to a reference Reynolds number, $Re = 3.5\times10^6$. Both Euler and Navier-Stokes calculations were carried out using high-order discretization. Note that

because there are no comparison data for this case, we rely on the performance on the ONERA grid to conclude that the accuracy for the aircraft simulation was also good. Therefore, the focus was placed on the ability to obtain converged results with the high-order procedures. The Euler grid consists of 6 blocks, each having $N_\xi \times N_\eta \times N_\zeta = 30 \times 71 \times 40 = 85{,}200$ grid points, with a total of 511,200. The largest grid spacing at the solid surfaces is $\Delta = 3 \times 10^{-3}$. The grid is shown in Fig. 21. For the Navier-Stokes mesh, 9 blocks were used, with the following grid points: fuselage $(80 \times 30 \times 50 = 120{,}000)$, nose cone $(31 \times 20 \times 50 = 31{,}000)$, tail cap $(31 \times 20 \times 50 = 31{,}000)$, wing base $(129 \times 43 \times 43 = 238{,}521)$, wing mid section $(50 \times 129 \times 44 = 283{,}800)$, wing tip (top) $(71 \times 41 \times 32 = 93{,}152)$, wing tip (bottom) $(71 \times 41 \times 32 = 93{,}152)$, wing patch $(61 \times 51 \times 51 = 158{,}661)$, and far-field grid $(73 \times 39 \times 48 = 136{,}656)$. This yields a total number of grid points of 1,185,942. The first grid at the wall is located at $\Delta y = 5 \times 10^{-5}$. The viscous grid and results are not presented in this paper.

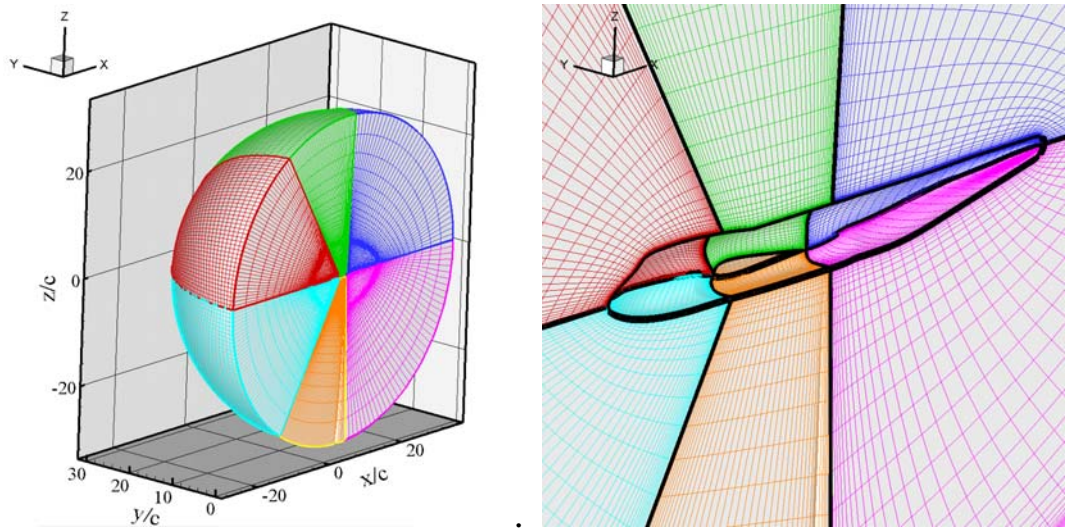


Figure 21 The Euler grid for Boeing 747-200 calculations

The Spalart-Allmaras turbulence model was used for the viscous calculations. The calculations proceeded without any difficulties and the residuals (Fig. 22) indicate convergence. Sample pressure contours are shown in Fig. 23. The shock location expected on the surface of the wing can be observed in the plots.

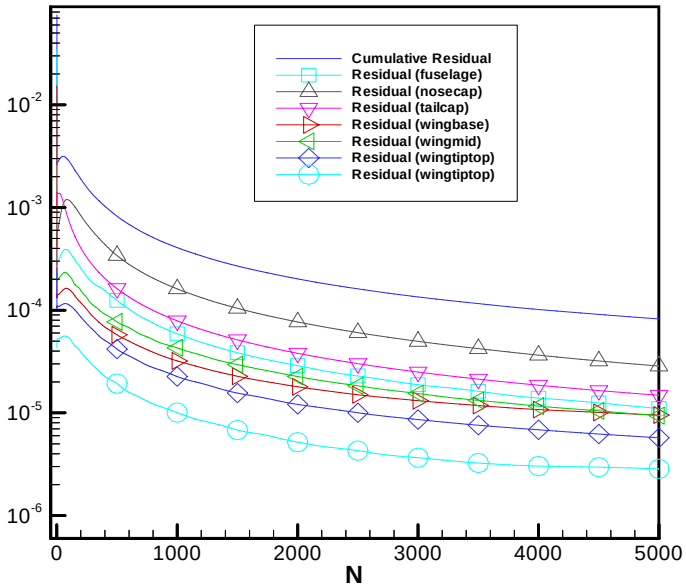


Figure 22 Early time temporal evolution of the residuals for high-order Euler simulation of flow over Boeing 747-200.

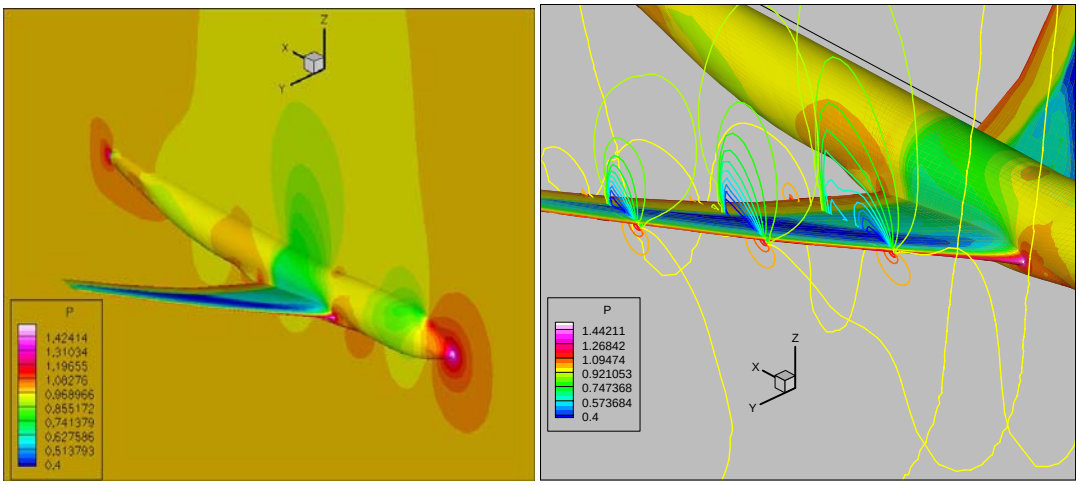


(a) (b)

Figure 23 Pressure field around the B747-200 (Euler simulation):
(a) Entire airplane (b) Shock compression on the wing.

Finally, in Fig. 24, we compare WENO and MUSCL results for the Boeing simulation for the same grid. It appears that the WENO results are more physical and therefore more accurate, though no test problems are available for this case.

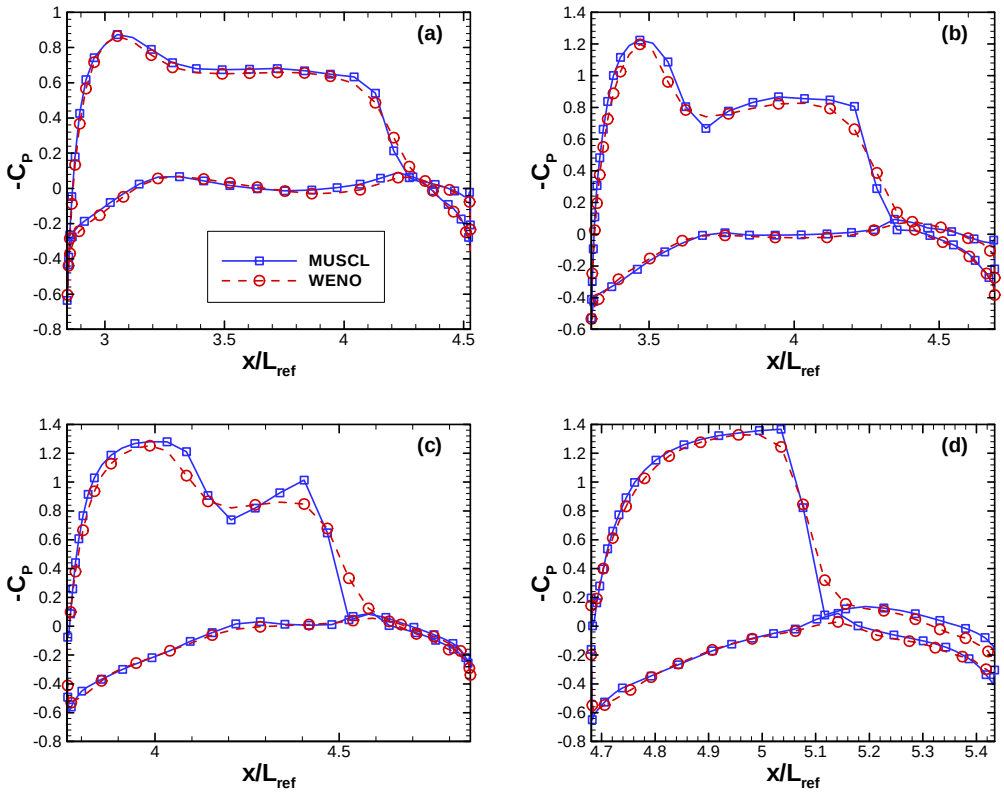


Figure 24 Profiles of the pressure coefficient from MUSCL and WENO Euler calculations at several wing sections of B747-200: (a) $y/L_{ref}$=0.5, (b) $y/L_{ref}$=1.0, (c) $y/L_{ref}$=1.5, and (d) $y/L_{ref}$=2.5. Here $L_{ref}$ is the pitch moment reference length.

## VI. Concluding Remarks

The challenges encountered in the implementation of high-order schemes for CFD simulation of realistic aerospace systems are described in this paper. Compared to low-order schemes, these challenges are associated with the generation of overlapped grid, the stricter mesh quality requirement, the excessive mesh refinement requirement, and additional complications in procedures that use filtering to quell the high wave number noise that is inherent in most CFD simulations. The two high-order schemes we have implemented are the compact and the weighted essentially non-oscillatory (WENO) schemes. The compact schemes have been developed for incompressible and low-Mach number flows, whereas WENO is intended for transonic, supersonic, and hypersonic flows. Because the geometries of interest are very complicated, and finite-volume methods are too expensive as candidates for high-order differencing as compared to finite difference procedures, curvilinear coordinate transformation with Chimera grids is an implicit part of the proposed technology. Unfortunately, the latter topic has not received enough attention for realistic aerospace systems.

Remedies for the various challenges described in this paper have been proposed and successfully implemented. This then allows us to illustrate some of the potential advantages of high-order method. It is important however to note that there is nothing new about the superior accuracy of high-order methods, since this has been demonstrated mathematically for the two procedures we are proposing. In this context, what is useful is the demonstration of superior accuracy for complex geometries. More work needs to be done on this topic, as we have only scratched the surface.

The authors envision a situation whereby, in some very complex geometries, the relatively inefficient generation of structured mesh, vis-à-vis the extra demands by high-order schemes, could force a localized use of high-order simulation, rather than its use everywhere in a computational domain. Regions with rich flow features (vortex shedding, massive separation, sound generation, etc.), could be solved with high-order methods, whereas a low-

order procedure might be sufficient in other parts of the solution domain. The implementation of this hybrid procedure is presently being undertaken.

## Acknowledgments

This research was funded by the United States Air Force, Contract F33615-03-C-3315, via the Phase II SBIR Program, with Dr. Datta Gaitonde as Technical Monitor. The authors are very grateful to the Air Force for giving Thaerocomp the opportunity to develop innovative research tools and to Dr. Gaitonde for the various administrative and technical supports.

## References

[1]Canuto, C., Hussaini, M. Y., Quarteroni, A. and Zang, T. A. 1987. Spectral methods in fluid dynamics, Springer-Verlag, Berlin/New York

[2]Lele, S.K. 1992 1992. Compact finite difference schemes with spectral-like resolution. *J. Comp. Phys.* 103, pp. 16-42.

[3]Tam, C.K.W. and Webb, J.C. 1993. Dispersion-relation-preserving finite difference schemes for computational acoustics *J. Comp. Phys.* 107, pp. 262

[4]Harten, A., Engquist, B., Osher, S. and Chakravarthy, S. 1987. Uniformly high order essentially non-oscillatory schemes, III, , *J. Comp. Phys.* 71, pp. 231-303.

[5]Liu, X. D., Osher, S. and Chan, T. 1994. Weighted essentially-nonoscillatory schemes, *J. Comp. Phys.* 115, pp. 200-212.

[6]Jiang, G. and Shu, C.-W. 1996. Efficient implementation of weighted ENO schemes, *J. Comp. Phys.* 126, pp. 202-228.

[7]Shu, C.-W., 1997, "Essentially Non-Oscillatory and Weighted Essentially Non-Oscillatory Schemes for Hyperbolic Conservation Laws," NASA CR-97-206253, ICASE Rep. No. 97-65.

[8]Gaitonde, D. and Visbal, M.R., "High-Order Schemes for Navier-Stokes Equations: Algorithm and Implementation intoFDL3DI", Technical Report # AFRL-VA-WP-TR-1998-3060, Air Force Research Laboratory, Wright-Patterson AFB, OH (1998).

[9]Visbal, M. R. and Gaitonde, D. V. 2002. On the use of higher-order finite-difference schemes on curvilinear and deforming meshes, *J. Comp. Phys.* 181, pp. 155-185

[10]Safta, C., Alabi, K. and Ladeinde, F., 2006, "Comparative Advantages of High-Order Schemes for Subsonic, Transonic, and Supersonic Flows," AIAA2006-0299.

[11]Adam, N. A. and Shariff, K. 1996. A high-resolution hybrid compact-ENO scheme for shock-turbulence interaction problems, *J. Comp. Phys.* 127, pp. 27-51.

[12]Weirs, V. G. and Candler, G. V. 1997. Optimization of weighted ENO schemes for DNS of compressible turbulence, AIAA 97-1940

[13]Germano, M, Piomelli, U., Moin, P., and Cabot, W.H., 1991, "A Dynamic Subgrid-Scale Viscosity Model," Phys. Fluids A **3**(7), 1760.

[14]Moin, P., Squires, K., Cabot, W.H., and Lee, S., 1991, "A Dynamic Subgrid-Scale Model for Compressible Turbulence and Scalar Transport," Phys. Fluids A **3**(11), 2746.

[15]Lilly, D., 1992, "A Proposed Modification of the Germano Subgrid-Scale Closure Model," Phys. Fluids A **4**, 633.

[16]Spalart, P.R., and Allmaras, S.R., "A one-equation turbulence model for aerodynamic flows," *La Rech. A'erospatiale,* V.1, 1994, pp.5-21.

[17]Strelets, M., "Detached Eddy Simulation of Massively Separated Flows," AIAA 2001-0879.
(Strelets, 2001)

[18]Menter, F.R., Kuntz, M., and Bender, R., "A scale-adaptive simulation model for turbulent flow predictions," AIAA 2003-0767.

[19]Shih, T.-H. and Liu, N.-S., "Partially resolved numerical simulation: from RANS towards LES for engine turbulent flows," AIAA 2004-0160.

[20]Shih, T.-H. and Liu, N.-S., "A unified strategy for numerical simulation of turbulent flows," *private communication*, 2005.

[21]Pulliam, H. T. and Chaussee, D. S. 1981. A diagonal form of an implicit approximate-factorization algorithm *J. Comp. Phys.* 39 (2), pp. 347.

[22]Ladeinde, F. 1995. Supersonic Flux-Split Procedure for Second Moments of Turbulence. AIAA Journal, Vol. 33, No. 7, pp. 1185-1195.

[23]Steffen, C. J. "A critical comparison of several low Reynolds number $k-\varepsilon$ turbulence models for flow over a backward-facing step. NASA Technical Memorandum 106173, Also AIAA-93-1927 and CMOTT-93-9, Presented at the 29th AIAA Joint Propulsion Conference and Exhibit, Monterey, CA, June 28-30, 1993.

[24]Driver, D. M. and Seegmiller, H.L. "Features of a reattaching turbulent shear layer in devergent channel flow," AIAA Journal, Vol. 23, No. 2. Feb. 1985, pp. 163-171.

[25]Schmitt, V. and Charpin, F. "Pressure Distributions on the Onera-M6-Wing at Transonic Mach Numbers," Experimental Data Base for Computer Program Assessment. Report of the Fluid Dynamics Panel Working Group 04, AGARD AR 138, May 1979.

[26]Anonymous (1998) NPARC Alliance Validation Archive Backwards-Facing Step: http://www.grc.nasa.gov/WWW/wind/valid/backstep/backstep01/backstep01.html, 1998.

[27]Jameson A., 1995, "Analysis and Design of Numerical Schemes for Gas Dynamics 1 Artificial Diffusion, Upwind Biasing, Limiters and Their Effect on Accuracy and Multigrid Convergence," RIACS Technical Report 94.15, Intl. J. of Comp. Fluid Dyn. 4, 171.
[28]Ladeinde, F., Cai, X., Visbal, M.R., & Gaitonde, D. 2001. Turbulence Spectra Characteristics of High Order Schemes for Direct and Large Eddy Simulation. *J. Applied Numerical Mathematics* Vol. **36** (2001), pp. 447-474.